micro

MDPI

Article

Exploring Microstructure Patterns: Influence on Hydrophobic Properties of 3D-Printed Surfaces

Mark Lohatepanont [1,†], Melody Chen [2], Luis Carlos Mendoza Nova [2], John-Thomas Murray [2] and Wilson Merchan-Merchan [2,*]

[1] Engineering Department, Swarthmore College, Swarthmore, PA 19081, USA
[2] School of Aerospace and Mechanical Engineering, University of Oklahoma, Norman, OK 73019, USA; melodychen256@gmail.com (M.C.)
* Correspondence: wmerchan-merchan@ou.edu
† Current address: Cornell University, Ithaca, NY 14850, USA; ml2828@cornell.edu.

Abstract: This study investigates the influence of microstructure patterns on the hydrophobic properties of surfaces of 3D-printed objects generated using photopolymer resin. Various arrangements and designs of microstructures on the surface of 3D-printed objects were examined. Leveraging the superior resolution of stereolithography printers (SLA) over fused deposition modeling, intricate microfeature designs were well-implemented. The experiments involved a range of structures on the surface of the 3D-printed objects, including precisely defined arrays of microcylinders, microchannels, and other complex designs generated by parametric equations. The hydrophobicity of the 3D-printed objects was assessed through the water droplet test, revealing a spectrum of results ranging from hydrophobic to weakly hydrophobic, and to hydrophilic surfaces. Light microscopy was employed to characterize the surface morphological properties of the 3D-printed objects, which were then correlated with the measured contact angles. It was discovered that the 3D-printed objects with microstructures formed using parametric functions exhibited patterns with irregularities and fluctuations along all directions or axes, resulting in a higher degree of hydrophobicity compared to structured matrices with pillared arrays. However, some surfaces created with parametric functions resulted in an anisotropic system where the material properties varied along one direction, while the other direction exhibited a flat, planar surface. These anisotropic systems were found to be less hydrophobic according to the water droplet test.

Keywords: hydrophobic surfaces; 3D-printed objects; light microscopy; anisotropic systems; contact angle

check for updates

Citation: Lohatepanont, M.; Chen, M.; Mendoza Nova, L.C.; Murray, J.-T.; Merchan-Merchan, W. Exploring Microstructure Patterns: Influence on Hydrophobic Properties of 3D-Printed Surfaces. *Micro* **2024**, *4*, 442–459. https://doi.org/10.3390/micro4030028

Academic Editor: Nurettin Sahiner

Received: 19 May 2024
Revised: 30 June 2024
Accepted: 10 July 2024
Published: 23 July 2024

Copyright: © 2024 by the authors. Licensee MDPI, Basel, Switzerland. This article is an open access article distributed under the terms and conditions of the Creative Commons Attribution (CC BY) license (https://creativecommons.org/licenses/by/4.0/).

1. Introduction

The fabrication and functionalization of surfaces with distinct wettability properties have significant interest in modern engineering due to their vast array of practical applications. Among these, hydrophobic surfaces stand out for their ability to repel water, a characteristic that allows for innovative solutions in sectors ranging from anti-corrosion coatings to anti-icing technologies. This paper explores the possibility of leveraging 3D printing technology to fabricate surfaces endowed with hydrophobic properties, a cutting-edge approach that could revolutionize the way we create materials with tailored surface characteristics.

To more concretely define a hydrophobic surface, a surface can be classified as hydrophobic depending on the contact angle (CA) that a droplet of water makes with its surface plane. There are generally three categories for hydrophobicity: a CA of $0° < \theta < 90°$ is considered hydrophilic (absorbs or dissolves water easily, or water-loving surfaces), a CA of $90° < \theta < 150°$ is considered standard hydrophobic (water-fearing surfaces), and a CA of $150° < \theta$ is considered superhydrophobic. Hydrophobic surfaces can also be further classified by their type: the Cassie–Baxter or Wenzel state. The Cassie–Baxter state is the conventional terminology for hydrophobicity where a droplet of water flows freely across

the surface of an object because in this state, the droplet of water floats slightly above the surface of the object and air bubbles are trapped below the droplet. This creates a composite air–material interface that leads to reduced adhesion and improved repellency. Wenzel state is when the water droplet adheres to the surface roughness and no air bubbles are trapped within. This means higher amounts of adhesion, and the liquid droplets are less likely to move. Both of these states can still exhibit hydrophobicity but via two different mechanisms [1,2].

Hydrophobic surfaces have importance in many physical applications and offer solutions in anti-corrosion and anti-icing applications. As such, there are currently many methods of making hydrophobic materials. The common method of producing these materials is generally in the form of hydrophobic chemical sprays, but these chemicals wear out and wash away, creating only a temporary solution for hydrophobic surfaces. Another method that is similar to what this study describes is placing microstructures on the surface.

Research has been devoted to diverse methods and techniques to create superhydrophobic surfaces [3,4], which are determined by their distinctive properties and applications that such materials offer. Traditional methods include nanoimprint lithography (NIL), plasma etching, chemical vapor deposition (CVD), electrospinning, and various combinations thereof. NIL involves a multistep process where a pre-etched stamp is used to create miniature architectures on a substrate [5]. Plasma etching bombards the substrate with energized gas ions to generate a rough surface [6–8], while CVD utilizes chemical and physical processes to coat the substrate with a structured layer that render the surface hydrophobic [9–11]. Electrospinning can produce a hydrophobic fiber mesh on the substrate's surface [12–14]. These techniques offer versatile approaches to achieve hydrophobicity on various substrates, contributing to advancements in hydrophobic material research. More recently, Rahman and Jacobi explored the use of micromachined hydrophobic surfaces for frost prevention and deicing on metal surfaces. The study showed that micro-milled grooves on metal plates exhibited hydrophobic properties [15]. More recently, research has expanded to study the fabrication of micropatterned surfaces through additive manufacturing or 3D printing to generate hydrophobic surfaces, conducted by several researchers [16–21]. Other innovative ways consist of altering the chemical and physical properties of either the surface or the sprays that are applied onto the surface; a few examples are using natural plant material, as proposed in the work of Lee and Kwon [22], or chemically via molecular etching, as described in the work of Vandencasteele et al. [23]. Recently, success has been demonstrated in the single-step approach that flames offer, directly converting the surfaces of various types of materials into possessing hydrophobic properties. The process is ultrafast, requiring only the introduction of the substrate into a tailored carbon-rich zone of the flame, which is ideal for forming C-layers on the surfaces of substrates [24–30].

Inspired by the studies focusing on manipulating micropatterned features across different surfaces to attain hydrophobicity, our research extends this concept by exploring the use of diverse microfeature shapes to render 3D-printed surfaces hydrophobic. The experimental scope ranged from defined microstructures, such as cylinders and channels, to those characterized by parametric equations.

2. Materials and Methods

To create hydrophobic microstructures, we utilized masked stereolithography (MSLA) 3D printing technology, known for its exceptional resolution and precision in fabricating intricate geometries. This capability makes MSLA ideally suited for producing complex micro-fixtures. In our study, we focused on cylinder grids, channels, and surfaces defined by cosine and sine waves.

The MSLA printer utilized in this work was the Elegoo Mars 3 4K. This MSLA printer is equipped with a 405 nm LED array capable of curing photopolymer resin with a layer resolution of approximately 25 μm. To achieve the desired surface topologies, the printer

settings were calibrated, with the layer height set to 50 µm to balance between the printing resolution and the time efficiency.

The resin 3D printing process began with a digital model of the desired object using Spaceclaim 2023 R2. This digital model was then sliced into thin layers using slicing software, which generated instructions (G-codes) for the printer to follow. The printer's build platform was lowered into a tank filled with liquid resin (Figure 1(a1)). The 3D printing process then commenced with the first film or layer of resin being exposed to UV light emitted by the LED array. This UV light initiated the solidification of the resin on the platform, forming the initial base of the object. Once solidified, the build platform moved incrementally (Figure 1(a1)), allowing fresh liquid resin to cover the solidified layer. The UV light then exposed the succeeding layer of resin as per the sliced pattern, solidifying it and bonding it to the layer beneath. This sequence repeated for each subsequent layer, gradually building up the object (Figure 1(a1)). This method resembles traditional fused deposition modeling in its layer-by-layer approach to 3D printing, with the distinction that material hardening occurs through light-induced polymerization rather than thermal processes. After printing, the samples underwent a two-stage post-processing procedure utilizing the Elegoo Mercury Plus, a system designed for both cleaning and curing 3D-printed parts. In the first stage, the samples were cleaned in a basin filled with 95% ethanol (Figure 1(a2)). The cleaning process was started by placing a model into a basin filled with 95% ethanol and running a vortex generator around the object for 15 min. This cleaning process dissolved the remaining non-hardened toxic resin, leaving the print mostly free of residue. After the cleaning process, the samples were exposed to UV light for approximately 15 min to achieve the final hardened state. Mercury Plus's vortex generator was used to ensure uniform exposure of the printed samples to the solvent, effectively removing uncured resin from their surfaces (Figure 1(a2)). Following the cleaning process, the samples were subjected to a curing stage on a rotating plate under a 405 nm UV light for 30 min. This post-curing exposure was timed to guarantee complete polymerization of the resin and ensure no toxic components were left on the print.

The resin selected for this experiment was a proprietary Elegoo UV-curable photopolymer, specifically formulated for high-resolution 3D printing. This material was chosen under the Elegoo's recommendation, which allowed detailed features that are essential for the successful implementation of hydrophobic microstructures. The resin used was standard photopolymer resin manufactured by Shenzen Elegoo Technology Limited (Shenzhen, China) and available through Elegoo. The exact composition can be found in the MSDS published by Elegoo; the major compositional elements are 3,3,5-trimethylcyclohexyl acrylate and 4,4′-Isopropylidenediphenol [31].

Models of the desired hydrophobic microstructures were created and expanded on based upon the microstructures found in the previous studies of Rahman and Jacobi [15]. The 3D-printed blocks were cubic and had physical dimensions of 20 × 20 × 20 mm. Each surface was designed with different surface geometries, including parallel microgrooves, pillar arrays, and randomized rough surfaces made using a combination of sinusoidal units, to explore their effects on hydrophobicity [15,32]. It is analogous to the work of Zhang and Resasco, who used various arrays or pillars of single-walled nanotubes to create hydrophobic surfaces; however, in this case, the arrays are created using a calcination process [33]. To further define the randomized rough surfaces, we used a combination of sine and cosine functions across a 2D surface, which, when summed, created a pseudo-random surface type. Concretely, a 1D version is described in Equation 1, where each of the constants $a_n \ldots g_n$ define arbitrary constants that vary the frequency, amplitude, and phase of each of the sine and cosine components.

$$f(x) = a_n \sin(b_n x + c_n) + d_n \cos(e_n x + g_n) \quad (1)$$

The expanded form of Equation (1) is Equation (2), which defines the pseudo-randomized form with arbitrary constants $a_n \ldots m_n$ implemented in this paper that define the surfaces

of the sample printed. Various forms of this equation were implemented with varying constants that generated a variety of different surface features.

$$Z = f(x,y) = a_n \sin(b_n x + c_n) + d_n \cos(e_n x + g_n) + h_n \sin(i_n y + j_n) + k_n \cos(l_n y + m_n) \quad (2)$$

These models were then exported to the MSLA printer for fabrication after being designed using the Spaceclaim 2023 R2 CAD software.

More accurate descriptions of the blocks can be observed the following Table 1, which shows a few examples of the equation with simple integer constants.

Table 1. Examples of three different parametric surfaces to demonstrate the construction of the surfaces using Equation (2).

(a) Z = cos (Y)	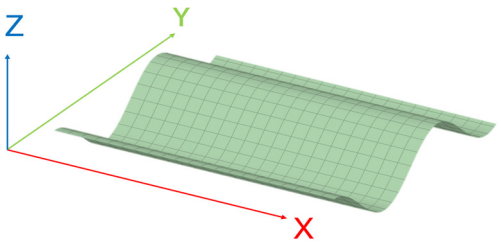
(b) Z = cos (X)	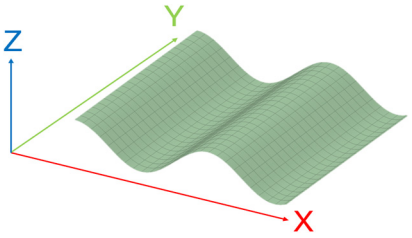
(c) Z = cos (X) + sin (Y)	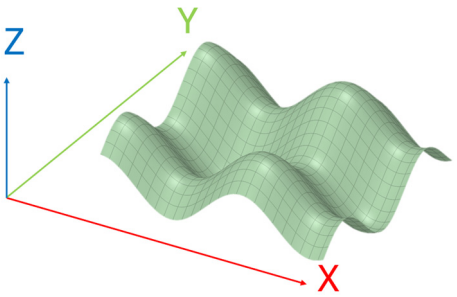

The graphs in Table 1 represent a few examples of Equation (2) being used with simple integer constants for a more accurate mathematical description of the blocks.

The upper row (a) shows a parametrically described surface, with the X and Y values ranging from 0 to 10 units, and the Z value being the value of the cosine of the X unit. It can be observed that this equation produces a cosine wave effect that is propagating in the Y direction. The middle row in Table 1b shows the same effect, except the value of the height (Z) is modified based on the cosine of X. The bottom row (c) combines the two effects to produce a rough surface that is used to describe the top of the blocks.

The hydrophobicity of the printed surfaces was evaluated by measuring the contact angle (CA) of water droplets placed on them. A camera was utilized to photograph a droplet of water deposited with a syringe delivering droplets of distilled water onto the surface of each sample. The samples were photographed from the three angles described in Figure 1(b1–b3).

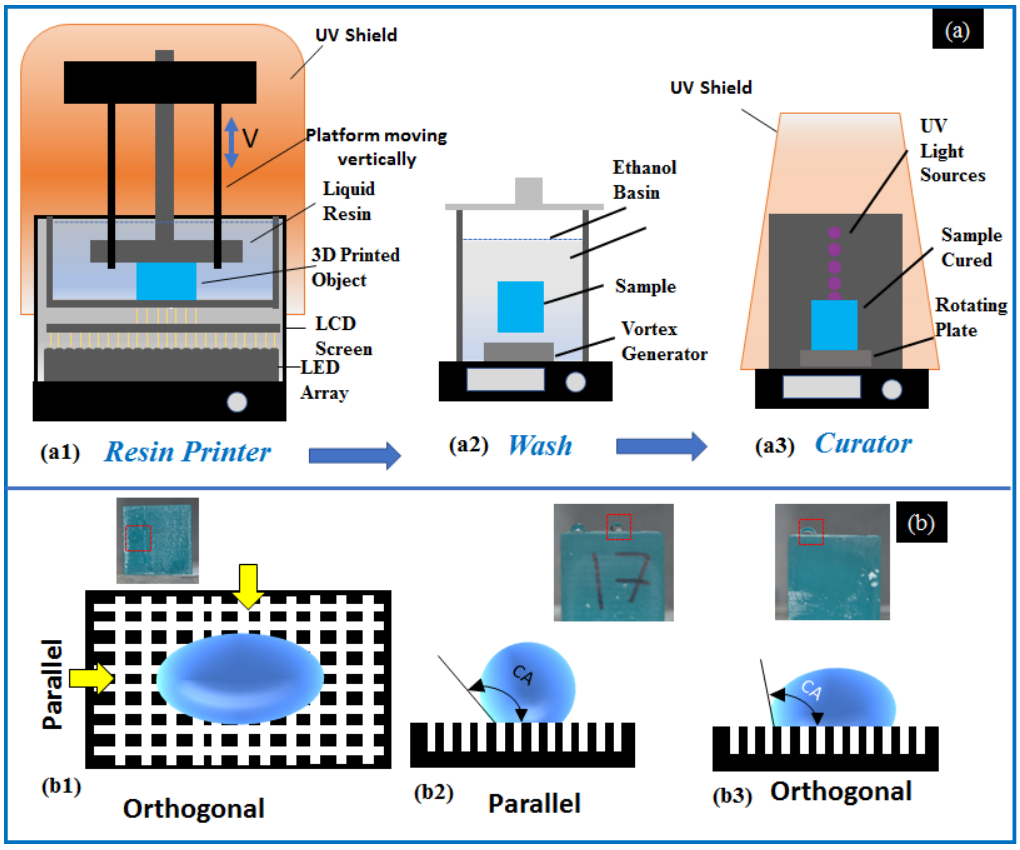

Figure 1. (**a**) The processes involved in masked stereolithography 3D printing, curing, and washing, and (**b**) the method used to image the contact angle of a water droplet on the 3D-printed surface when viewed from (**b1**) the perpendicular view from the top, (**b2**) parallel, and (**b3**) orthogonal directions. A dotted frame in each photograph encloses a representative water droplet resting on the engineered surface.

Following the photography process, the images collected were post-processed, and then, using goniometer software, the CA was attained. The CA was collected as the maximum of the parallel and orthogonal CAs. The CA was measured with at least three measurements taken for each sample to ensure accuracy and reproducibility.

Based on the measured CAs, the surfaces were classified into hydrophilic, standard hydrophobic, and superhydrophobic categories. Additionally, the Cassie–Baxter and Wenzel states can be inferred from the droplet behavior and surface morphology. Furthermore, surface analysis of the 3D-printed objects was performed via a Keyence Digital Microscope (VHX-7000 Keyence Ultramicroscope, Keyence Corporation of America, Itasca, IL, USA), where we were able to observe the surface structures and obtain a surface roughness analysis. Additionally, for further image clarity on a micro-scale, a scanning electron microscope (SEM) was used to capture high-resolution images of the surface of the blocks. Prior to placement in the SEM chamber, the resin blocks were treated with a sputter coater (Emitech K-575D, Ashford, UK) for about 16 seconds, resulting in the deposition of a very thin layer (~4 nm) of iridium (Ir) on their surfaces. The SEM employed for analysis was the Thermo-Quattro S-field-emission environmental scanning electron microscope (FE-ESEM), produced by Thermo Fisher Scientific (Waltham, MA, USA).

3. Results and Discussion

The hydrophobic properties of the 3D-printed surfaces were evaluated through CA measurements, a direct indicator of hydrophobicity. The results reveal significant variations in the CAs, ranging from 51° to 147°, depending on the microstructural geometry of the surface. The surfaces designed with a randomized structure seemed to exhibit nearly supe-

rior hydrophobicity (CA > 150°), with their CAs consistently exceeding 100°, categorizing them as hydrophobic (CA > 90°). In contrast, the surfaces with simpler, less complex microstructures demonstrated CAs within the 40° to 100° range, leading to a variety of levels of hydrophobicity. To compare the CAs of the engineered blocks, a 3D-printed sample with no microstructures underwent the water droplet test and served as a control block. This block achieved a contact angle of 57°.

3.1. Sample Analysis

To study the effect of the microstructure's shape on the hydrophobic properties of the 3D-printed objects, objects with a variety of different microstructure were designed and 3D-printed. Figure 2 presents the surface of a 3D-printed object defined in two dimensions with sinusoidal waves. Figure 2(a1) presents an isometric view of the CAD generated sinusoidal object, and the digital light microscope imaging analysis shows that along all three axes or directions features with similar irregularities and fluctuations were present (Figure 2(a3–a5)). The periodicity and amplitude can be observed in the light micrographs in Figure 2(a3–a5). Figure 2(a6,a7) display the surface roughness and structure perpendicular to the reference plane. The isometric images in Figure 2(a6-1,a7-1) display the stereoscopic shape "or slicing" and the cross section of the selected profile or area on the surface of the object. Figure 2(a6-3,a7-3) graphically display the roughness across the planes. The surface of the 3D-printed object, created with sinusoidal waves, resulted in symmetrical microstructures with rounded or blunted peaks (Figure 2(a1–a4)). It is interesting to observe the spectacular pattern of the microstructures created using the sine function and a relatively inexpensive 3D printer.

The extruding structures from the surface of the 3D-printed object were continuous and smooth, without abrupt changes in direction or magnitude (Figure 2(a3–a6)). The surface morphonology of this block exhibited isotropic properties. The contact angle of a water droplet placed on the surface of the object created with sinusoidal waves was 115° for both the parallel (Figure 2(a8)) and orthogonal directions (Figure 2(a9)). Figure 2(a10) shows an image from top view of a droplet resting on the surface of the 3D-printed object. Figure 2(a11–a13) are SEM images of the 3D-printed surface. The roughness and variation in surface topography can be visibly discerned, by the change in contrast of the SEM images, as darker colors represent a lower height and the lighter values a higher height.

The surface of a 3D-printed block with crossed arrays of square-shaped pillar microstructures was prepared and tested for hydrophobic properties (Figure 3). The protruding rectangular prisms has a face length of 100 μm and depth of 600 μm. "Crossed" indicates that this pattern repeats in each of the X and Y directions, resulting in a grid-like pattern.

Figure 3(a1) displays a view of the CAD-generated arrays with a selected magnified area (Figure 3(a2)). The arrays were equally spaced in both directions, as observed in the micrographs (Figure 3(a3,a4)). However, the isometric view of the targeted area for the roughness measurement (Figure 3(a5–a7)) under the light microscope reveals a pattern where one direction displays a flat, planar surface, while the orthogonal direction exhibits fluctuations. Significant differences in certain features are observable when comparing the surfaces of the 3D-printed objects created using a sinusoidal function with those created using an array of pillars with a squared cross-sectional area. The squared pillars' surface exhibited a rougher texture along one axis compared to the other side (Figure 3(a6,a7)). The difference in roughness between the two directions is indicated by the amplitude profiles displayed in Figure 3(a6,a7). A critical difference pertains to the contact angle of the texted water droplet. The water droplet placed on the surface of the object with the squared pillar arrays extended as if along a longer axis (Figure 3(a10)). The contact angle was measured to be 118° (parallel) and 106° (orthogonal), as shown in Figure 3(a8,a9), respectively. Figure 3(a11–a13) show SEM images of the 3D-printed surface. Each individual grid section can be seen, along with smaller imperfections around the pillars.

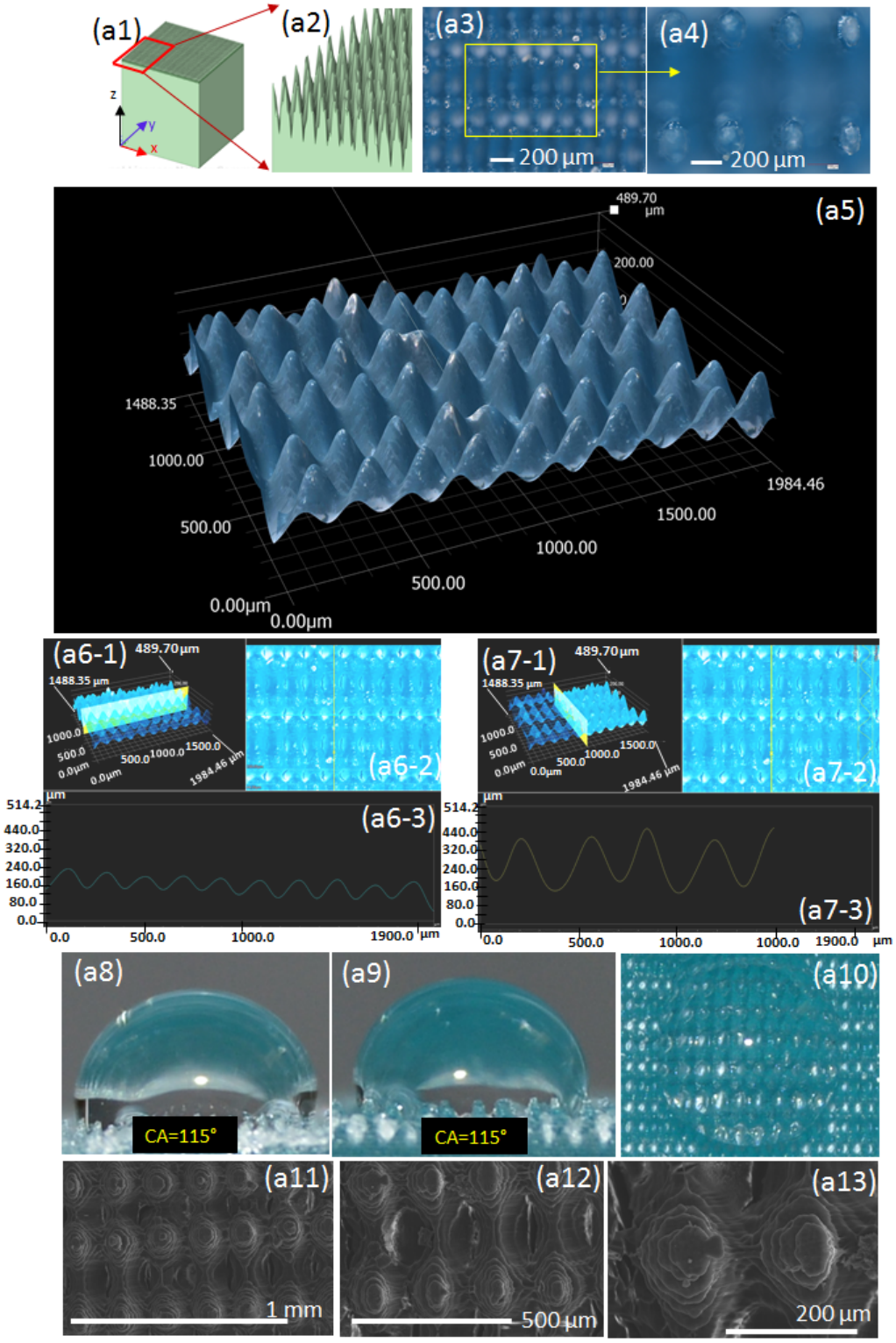

Figure 2. Light and SEM microscopy images showcasing surface morphology, along with a water droplet test conducted on a 3D-printed object featuring a parametrically defined surface with equation $Z = 0.11 * \sin(100x) + 0.31 * \cos(32x) + 0.1 * \sin(30y) + 0.31 * \cos(20y)$. Figures (**a1**,**a2**) depict CAD-generated fixtures on a parametrically defined surface; (**a3**–**a7**) showcase light microscopy images, including 'slicing' along the cross-section in both directions; (**a8**–**a10**) present photographs of a water droplet; and (**a11**–**a13**) illustrate SEM images. (**a6-1**–**a6-3**) and (**a7-1**–**a7-3**) display the stereoscopic shape 'or slicing' and the cross-section of a selected area created by sinusoidal waves on the object's surface along orthogonal and parallel planes, respectively.

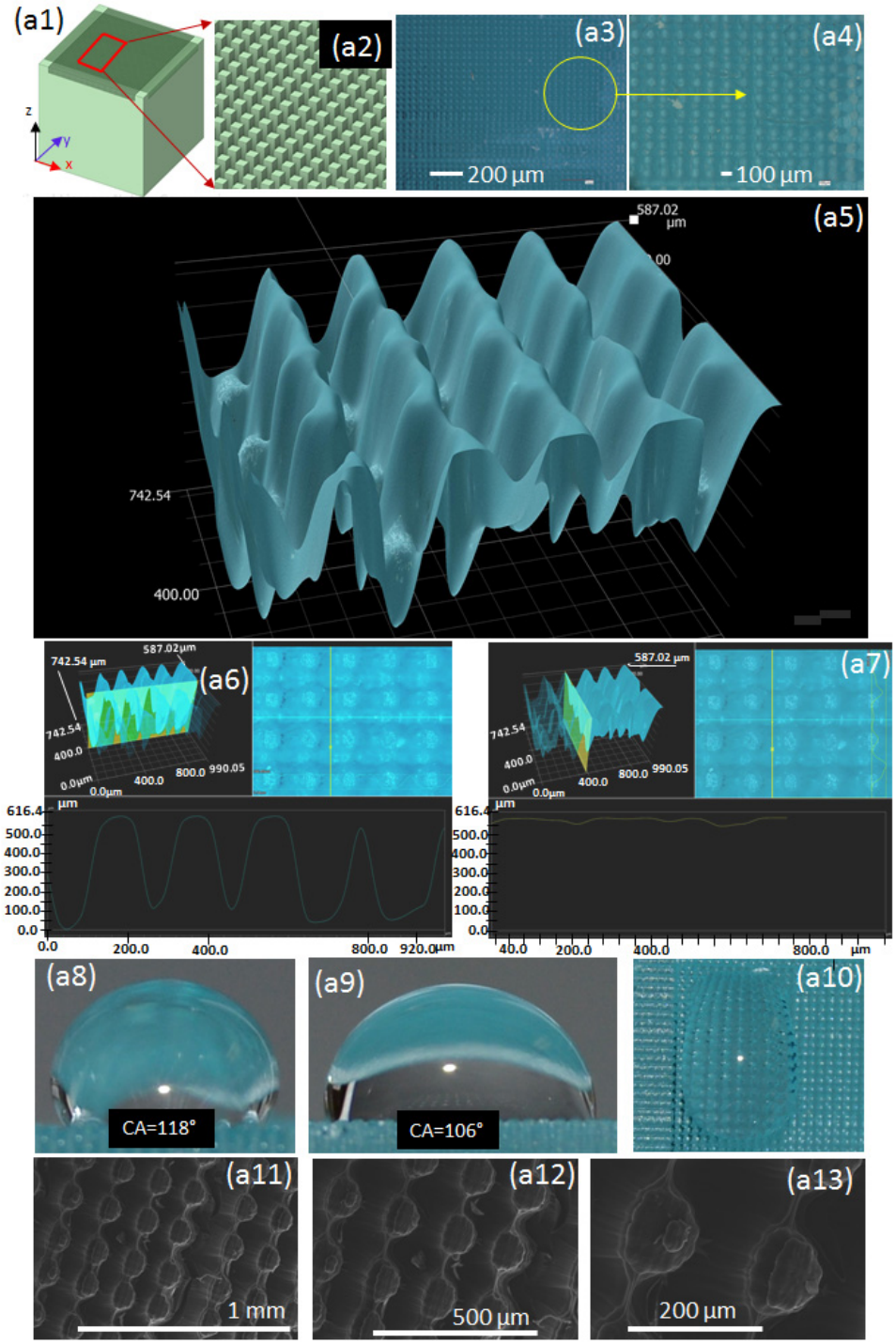

Figure 3. Light and SEM microscopy images showcasing surface morphology, along with a water droplet test conducted on a 3D-printed object with a structured matrix of pillared arrays 100 um apart and 600 um deep. Figures (**a1**,**a2**) display CAD-generated fixtures of pillared arrays; (**a3**–**a7**) feature light microscopy images, including 'slicing' along the cross-section in both directions; (**a8**–**a10**) include photographs of a water droplet; and (**a11**–**a13**) portray SEM images that clearly identify details of the pillared arrays on the engineered surface.

The surface of the 3D-printed block with features formed using a pseudo-random cosine and sine wave pattern was prepared and tested for its hydrophobic properties (Figure 4). As observed in both the CAD graphics and digital microscope images, the surface exhibited an

anisotropic property. Specifically, along the Y direction, it featured a flat, planar surface, while in the other direction, irregularities were present (Figure 4(a1–a5)).

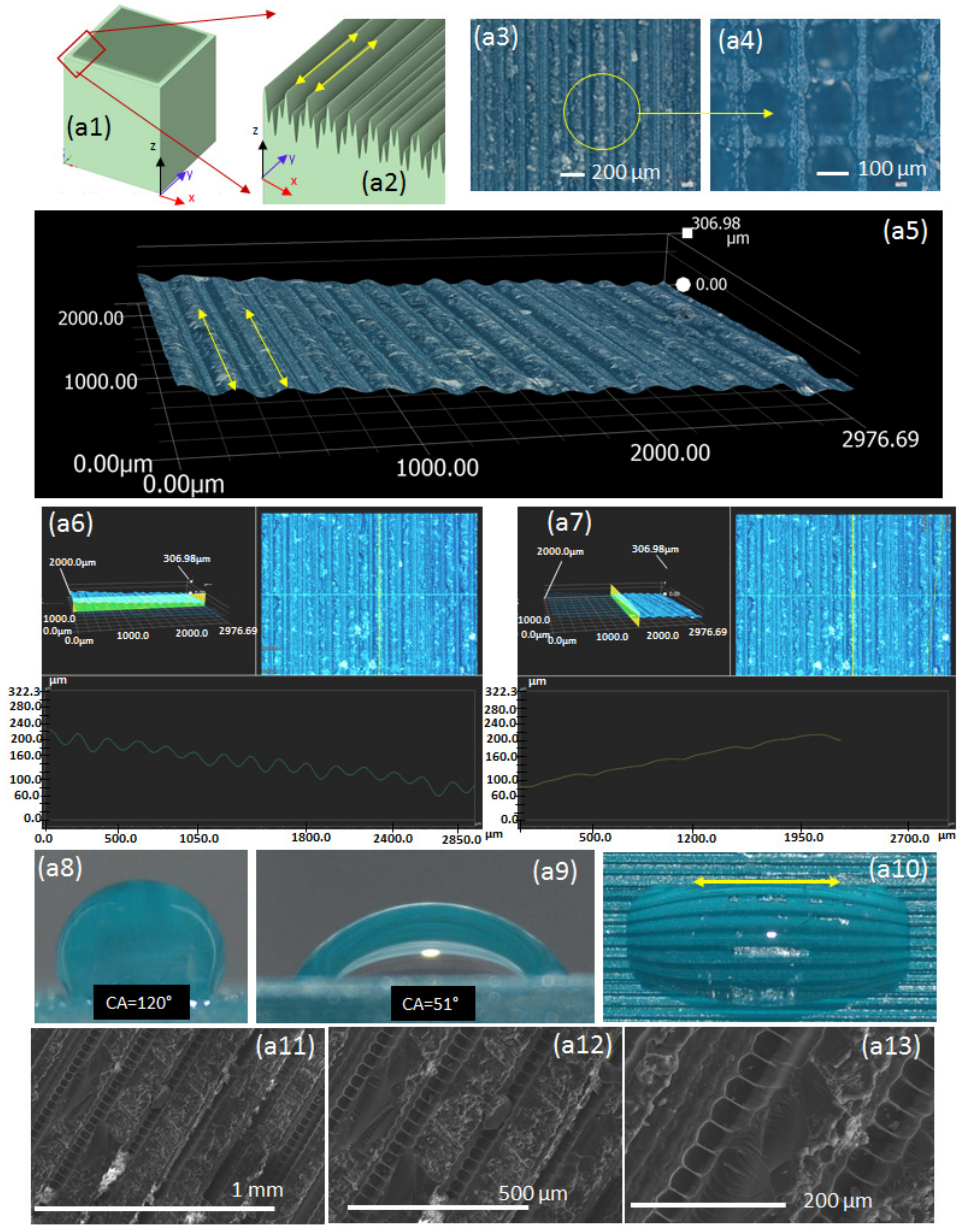

Figure 4. Light and SEM microscope images showcasing surface morphology, along with a water droplet test conducted on a 3D-printed object formed using the parametrically defined equation $Z = 0.11\sin(100x) + 0.11\cos(32x)$. Figures (**a1**,**a2**) display CAD-generated parametric fixtures on the engineered surface; (**a3**–**a7**) feature light microscopy images, including 'slicing' along the cross-section in both directions; (**a8**–**a10**) include photographs of a water droplet; and (**a11**–**a13**) highlight details of the engineered microstructures collected by SEM.

Figure 4(a6,a7) display the profile area in the horizontal and vertical directions. The CA in the parallel arrangement was 120°, compared to 51° in the orthogonal direction. The pattern uniquely affected the CA, creating a surface displaying hydrophobicity in one direction (CA 90° < θ< 150°) and a hydrophilicity in the other direction (CA 0° < θ < 90°). Figure 4(a11–a13) shows similar surface topologies as in Figure 2(a11–a13), where the surface can be observed to be rough, with no clear repetition of the surface structures.

Figure 5 showcases a block that features a surface formed by a one-dimensional modulated sine wave. The modulated sine wave created an alteration in the amplitude,

resulting in deeper peaks and much closer spacing than those created by the sine wave in the block in Figure 4.

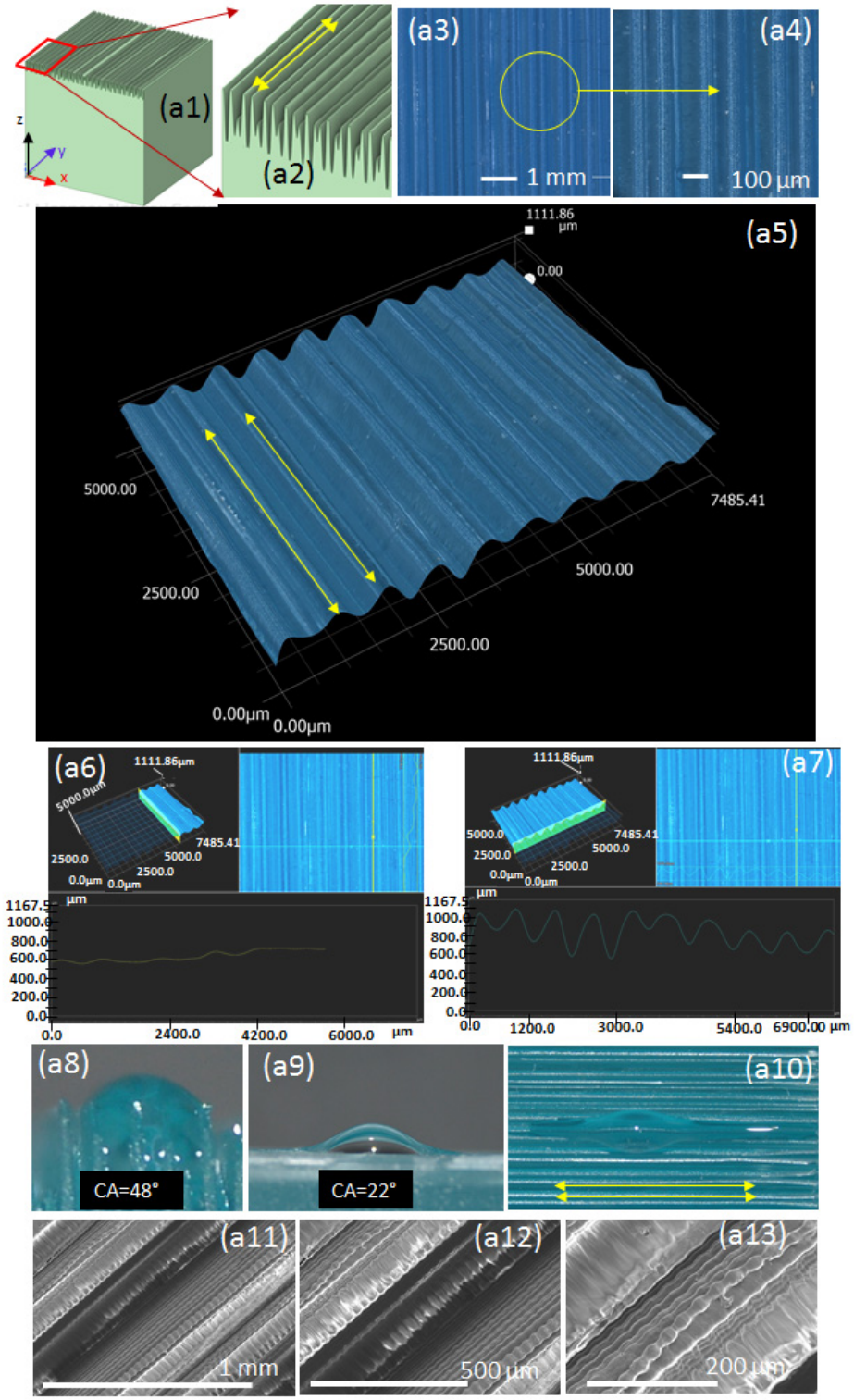

Figure 5. Light and SEM microscope images showcasing surface morphology, along with a water droplet test conducted on a 3D-printed object formed using the parametrically defined surface Equation $Z = \sin(\sin(23x + 0.33) + \cos(15x + 0.43))$. Figures (**a1**,**a2**) depict CAD-generated fixtures on a parametric defined surface; (**a3**–**a7**) showcase light microscopy images, including 'slicing' along the cross-section in both directions; (**a8**–**a10**) present photographs of a water droplet; and (**a11**–**a13**) illustrate SEM images.

Figure 5(a5–a7) show the structural morphology and general composition of the surface of the block. While there are variations, likely created by the 3D printing manufacturing process, between the actual block and the CAD design, the general surface likeness is imitative. It should be noted that the magnification employed in the digital microscope was significantly increased for this block to better observe the details of the waved structure.

Unlike in block shown in Figure 4, the surface of the block in Figure 5 was superhydrophilic across all directions and was unable to support a water droplet, as the droplet spread out extensively and quickly upon contact (Figure 5(a8–a10). Figure 5(a11–a13) present additional SEM microscope images. The one-dimensional surface structures are visible, as all the surface features travelled upward, from left to right. This caused the water droplets to be hydrophobic only in one axis.

This leads to the following theory: microstructures displaying hydrophobic properties should not only have random surface features but also a high resolution. It appears that the most crucial aspect is maintaining a non-consistent average surface height on a micro-scale. However, on the macro-scale, heights should remain consistent enough to ensure the repeatability of patterns, thus maintaining the surface's hydrophobicity. This theory is examined in the next section.

3.2. Contact Angle Analysis

Figure 6 presents a compilation of the 3D-printed blocks with various patterns on the surface with a conducted water test for hydrophobicity. The figure is arranged from top to bottom in ascending order of the average roughness for a portion of the samples investigated; roughness values across different axes show the roughness for each axis.

Figure 6(1a–5a) illustrate the overall trend of an increasing contact angle in correlation with the average surface roughness. Notably, this trend deviated at the instances represented by the blocks in Figure 6(6a,7a), which are distinguished from the remainder by their unique microstructural configuration. Specifically, the blocks in Figure 6(6a,7b) exhibit a circular grid pattern with varying heights, a structural characteristic that, despite contributing to an increased roughness, appears to inadequately support the maintenance of the water droplet surface tension.

This suggests that the uniform grid pattern, while enhancing surface roughness, does not effectively facilitate high contact angles due to its inability to adequately support the water droplet. In contrast, the blocks in Figure 6(1a–5a), which feature pseudo-random cosine and sine wave patterns, demonstrate a different interaction with the water droplet. The undulating surface contours of these blocks create a cradling effect, akin to a bowl that gently supports the water droplet. This structural support prevents the disruption of the surface tension, thereby enabling the droplets to sustain higher contact angles. This phenomenon underscores the critical role of microstructure geometry in influencing hydrophobic properties, suggesting that not only the surface roughness, but also the specific pattern and type of microstructure significantly affect water droplet support and the resultant contact angle measurements.

To further explain why some microstructures do not support hydrophobicity, in Figure 6(6a–7a), the intended design had a high roughness, which theoretically means that the surface should be hydrophobic. However, the results show that this structure was not hydrophobic. This could be because, while there was a sufficient difference in height from the top of the tallest feature down to the bottom of the surface, the majority of the surface was still flat, and this left most of the surface relatively flat. This indicates that while the surface roughness may have been increased, the surface itself did not have enough features to be hydrophobic.

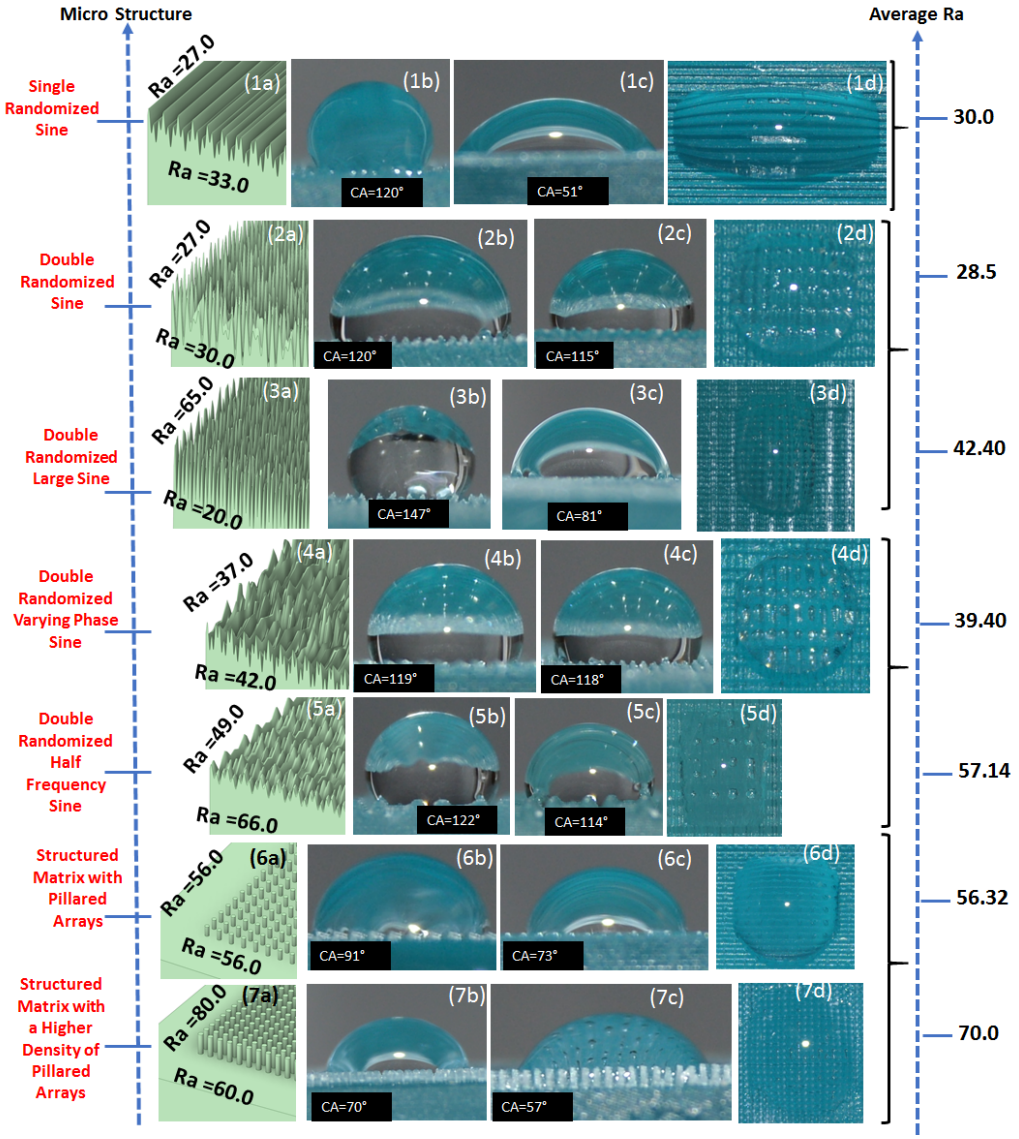

Figure 6. (**1a–7a**) Collection of CAD renderings used for 3D-printed objects. (**1b–7b**), (**1c–7c**) Corresponding contact angles of a water droplet test in the parallel and orthogonal directions. (**1d–7d**) The water droplet from the perpendicular view from the top as it sits on the surface of the object.

It could be hypothesized that significantly increasing the surface roughness involves fully populating the surface with highly irregular features. This contrasts with the surfaces shown in Figure 6(6a–7a), where roughness was achieved using large, extruded pillars with empty voids between them. By eliminating these voids and filling them with equally rough surfaces, we mitigated the effect of flat spaces and prevented the overall loss of hydrophobicity. This approach was implemented in the creation of parametrically defined surfaces, where each section was crafted to be sufficiently rough, ensuring no voids between the microstructures. This ensured that the water droplets would be adequately supported by the microstructures in all directions and could not collapse into any imperfection. This is supported by Haishuo Liu et al. [34], who similarly produced a grid of large pillars but with a higher resolution, which left minimal space between the pillars. This has the same effect as filling the empty flat space with parametrically defined surfaces, as carried out in our study. Both these approaches minimized the empty space and led to an increase in the contact angle of the water droplet, indicating a higher level of hydrophobicity. Furthermore, by increasing the surface roughness in a way that eliminates large voids, the surface can more effectively trap air pockets beneath a water droplet, supporting the droplet's surface tension.

With low-resolution pillars, when a water droplet lands on them, air escapes through the open voids, causing the droplet to break at the corners of the pillars and fall into the voids. However, with smaller and self-contained air pockets, the water droplet immediately and completely covers them, leaving no room for the air to escape. This trapped air adds a force that ultimately supports and maintains the water droplet's surface tension.

3.3. Comparing Roughness and Contact Angle

The plot in Figure 7 illustrates a deeper look into the average roughness and contact angle of various 3D-printed patterns. The water droplet test revealed (i) the pattern of the microstructures and that (ii) in certain patterns, the distances, depths, and sizes of similar patterns can influence the hydrophobicity of the 3D-printed objects.

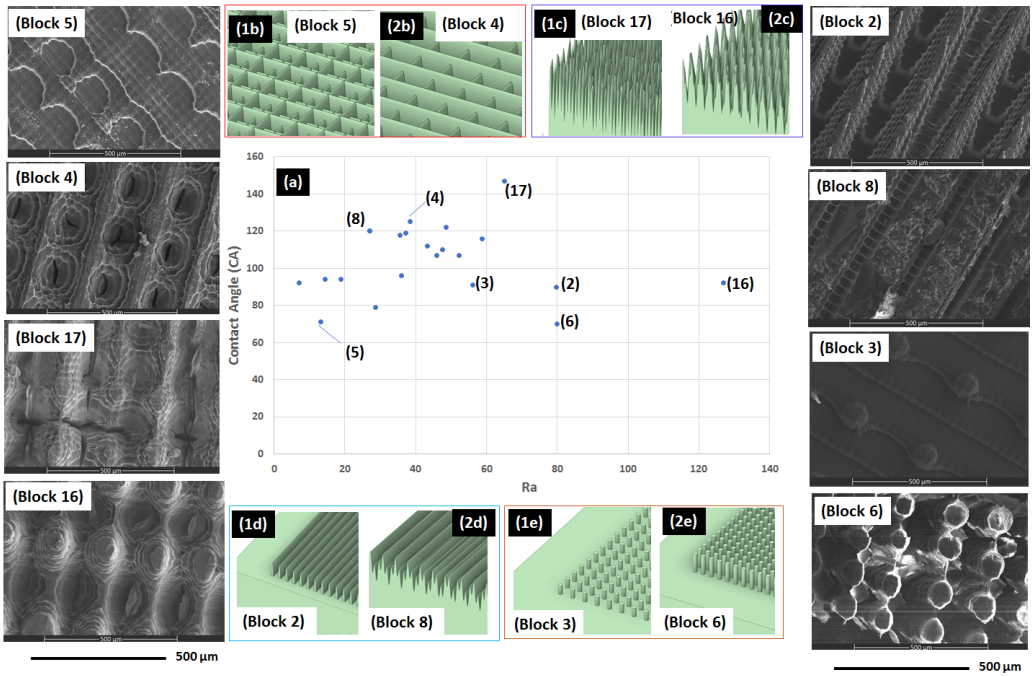

Figure 7. Plot displaying the correlation between the surface roughness (Ra) and the contact angle conducted on the various 3D-printed objects. (1b, 2b, 1c, 2c, 1d, 2d, 1e, and 2e) represent the renderings of selected CAD designs with patterns of the different microstructures. The SEM images in the left column (labeled as Block 4, 5, 16 and 17) depict the surface morphology corresponding to the CAD designs in the top row, while those in the right column (labeled as Block 2, 3, 6 and 8) correspond to the CAD designs in the bottom row.

For instance, the patterns in the blocks of Figure 7(1b,2b) are related. Both blocks are crossed microstructures with a width of 100 µm. The major difference in structure between the blocks is the oscillating Z microstructure of 275 µm. However, one resulted in hydrophobicity, and the other in hydrophilicity (Figure 7(1b,2b)). Similar trends were observed for the other patterns. The diameters of the pillars in block 3 (Figure 7(1e)) and block 6 (Figure 7(2e)) were the same, at 100 µm. However, there was a difference in the pillar depth: block 3 had a depth of 300 µm, while block 6 had a depth of 100 µm. Reducing pillar depth appeared to negatively affect the hydrophobicity property of the 3D-printed block (Figure 7(1e,2e)).

It is difficult to discern blocks formed of similar patterns by simple eye inspection. For instance, considering block 17 and block 16 in Figure 7(1c,2c), respectively. Although both blocks were generated from a sinusoidal function, their hydrophobic properties significantly varied. Block 16 was created using a double randomized larger cosine amplitude, while block 17 was created using a double randomized larger sine amplitude. The block formed using the sine amplitude exhibited excellent hydrophobic properties compared to the one formed using the cosine function (see Figure 7(1c,2c)).

The contact angles presented in Figure 7a were obtained from the water droplet test and indicate the measurement with the higher contact angle.

The scatter plot presented in Figure 7a reveals more experimental correlation between the surface roughness (Ra) of the printed samples and their water contact angles (CAs). The Ra, arithmetic average roughness, is a measure of the average deviation of the roughness profile from the mean line or centerline within a sampling length. It is calculated by averaging the absolute values of the height deviations from the mean line over the evaluation length. The Ra provides a general indication of the roughness of a surface. The data points in Figure 7a suggest an initial positive correlation: as the surface roughness increases, there is a tendency for the contact angle to increase as well. This correlation aligns with the widely accepted theory that micro-scale and nano-scale surface roughness enhances the hydrophobicity of a material by trapping air and reducing the liquid–solid contact area, thus increasing the CA. The roughness of each of the samples generally increased over the blocks generated with more complex shapes, like those generated by the pseudo-random sinusoidal structures.

The plot also shows that sinusoidal structures have the capability to produce consistently hydrophobic surfaces, with the majority of the pseudo-random sinusoidal blocks landing within an average roughness between 40 and 70.

There are three outliers to the positive correlation between the average roughness and the CA within average roughness values between 80 and 126. These values correspond to samples or block with cylindrical microstructures (Figure 6(7a)), a block with a single channel microstructure, and that from one of the pseudo-randomized blocks with the surface described by Equation (3).

$$f(x, y) = 0.11 * \sin(100x) + 0.31 * \cos(32x) + 0.1 * \sin(30y) + 0.31 * \cos(20y) \quad (3)$$

A possible reasoning to the outlier points are that (i) they are relatively simple structures, that is, an outliner point belonging to a simple replica of 100 um pillars is a much simpler structure that is unlikely to fully support the water droplets; (ii) meanwhile, the profile of a structure with high roughness from a randomized sine is simple.

To further investigate the reasoning behind this outlier, we can look at the light microscope surface profiles of a block (e.g., a low performance block, such as block 16 in Figure 7), formed using a double randomized large cosine amplitude (Figure 8(a1–a5)) compared to a higher performance hydrophobic block (block 17 in Figure 7), formed using a double randomized large sine amplitude (Figure 8(b1–b5)).

The 3D-printed block using the cosine function resulted in an Ra (arithmetic average roughness) of 96.21 µm and an Rz (average roughness) of 337.84 µm (Figure 8(a1–a5)). The object formed with the sinusoidal sine function resulted in an Ra of 78.15 µm and an Rz of 261.73 µm (Figure 8(b1–b5)). That is, there were differences in the Ra and Rz of 16.93% and 25.40%, respectively. The parameter Rz measures the average peak-to-valley height of the roughness profile within a sampling length. The Rz provides information about the height variations on the surface and is useful for assessing the depth of surface irregularities. The roughness of the cosine block (Figure 8(a1–a5)) was, to some extent, larger than that of the sine function, but not significantly. The structures of the cosine block were more uniform in height (Figure 8(a3)); however, the block formed with the sine function had features of two different heights (arrows in Figure 8(b3)). Although the roughness value was smaller, it had multidimensionality (the height of the features varies), and it appears to be an important parameter for making this surface more hydrophobic. That is, it resulted in a more inconsistent and "rough" type surface with higher variation and peaks and troughs. A similar analysis can be applied to all the other 3D-printed objects. Furthermore, the SEM images in Figure 8 (a6,b6) show the roughness of the surface at a micro-level. The micro-scale roughness depicted in the SEM images more accurately represent the individual section roughness better than the global scale surface scan, as shown in Figure 8(a3).

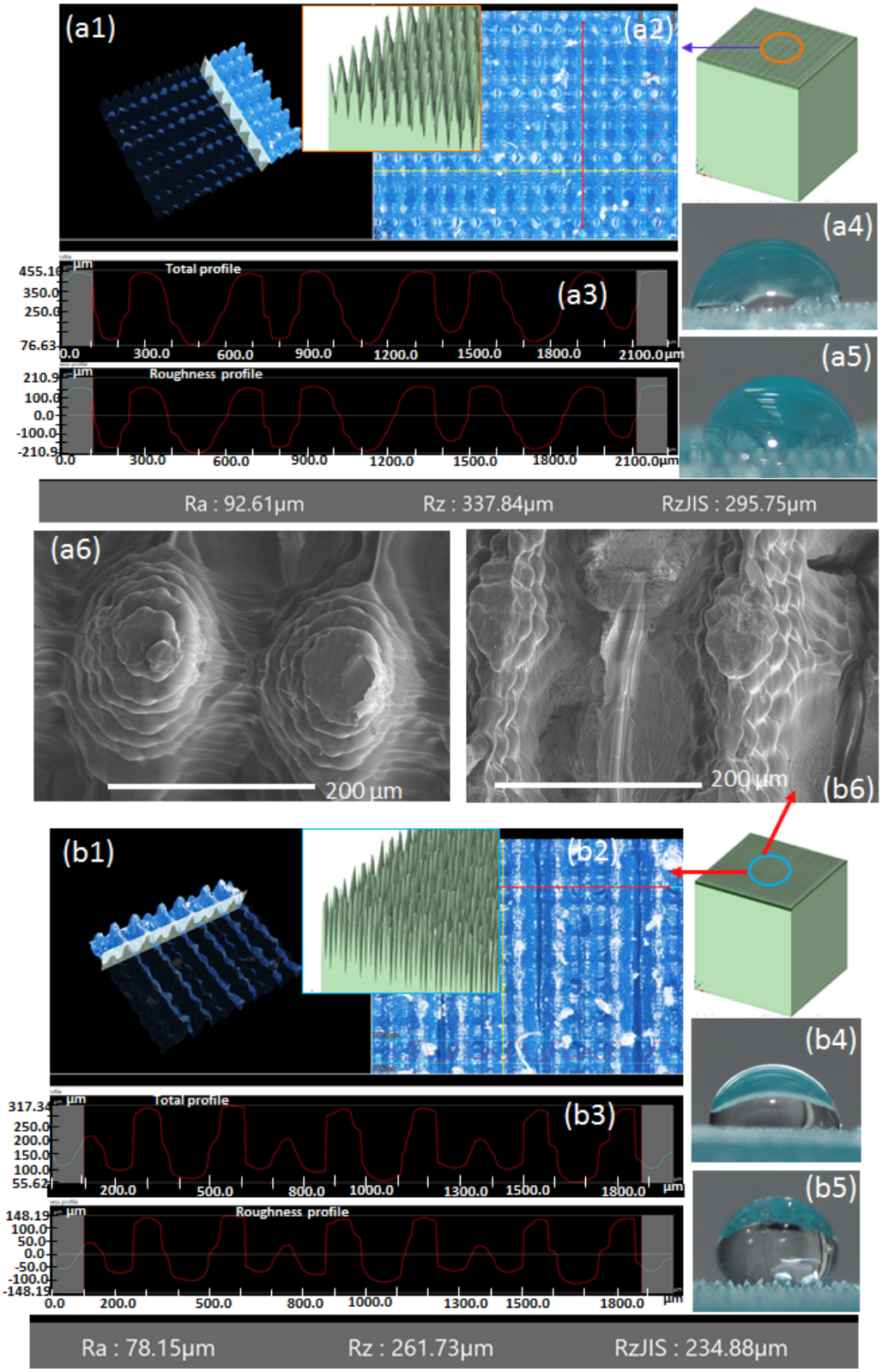

Figure 8. (**a1**–**a3**) Light microcopy and SEM images of the surface roughness of a block formed using a cosine function including 'slicing' along the cross-section in both directions. (**b1**–**b3**) Light microcopy and SEM images of a block formed using a sine function including 'slicing' along the cross-section in both parallel and orthogonal directions. The photographs (**a4**,**a5**,**b4**,**b5**) represent the water droplet test conducted on the 3D-printed objects along both directions. (**a6**,**b6**) represent details of the microstructure patters of the cosine and sine function obtained by SEM analysis, respectively.

4. Conclusions

This investigation into the influence of micro-structured surfaces on hydrophobicity, fabricated using MSLA 3D printing, provides substantive insights into the roughness requirements and a possible surface equation that can be applied to producing hydrophobic surfaces. The results indicate that while increased surface roughness is conventionally linked to enhanced hydrophobicity, the contact angle, a quantifiable measure of hydrophobicity, is majorly influenced by the microstructural design of the surface and minorly by the average surface roughness.

The empirical data depicted in the results show a predominant trend where increasing roughness correlates with larger contact angles, but some deviations observed in specific samples underscore the importance of the microstructural geometry. Surfaces with pseudo-random cosine and sine wave-type microstructures demonstrated a superior capacity to support water droplets, resulting in higher contact angles. This effect suggests the emergence of a possible Cassie–Baxter state, which is desirable for hydrophobic applications.

Future research should concentrate on carefully creating and adjusting the shapes and patterns on surfaces to better understand how these details affect hydrophobicity. It will also be important to test how durable these 3D-printed surfaces are over time and in different environments to ensure real-world applications are viable. The outcomes of this research could have significant effects on numerous fields, including the development of waterproof materials and surfaces that resist dirt and grime, potentially leading to new advances in the field of materials science and engineering.

Author Contributions: Conceptualization, M.L., M.C., L.C.M.N. and W.M.-M.; methodology, M.L., M.C., L.C.M.N. and W.M.-M.; software, M.L.; validation, M.L., M.C., L.C.M.N. and W.M.-M.; formal analysis, M.L., M.C., L.C.M.N. and W.M.-M.; investigation, M.L., M.C., L.C.M.N. and W.M.-M.; resources, W.M.-M.; data curation, M.L., M.C. and W.M.-M.; writing—original draft preparation, M.L., M.C., L.C.M.N., J.-T.M. and W.M.-M.; writing—review and editing, M.L., M.C., L.C.M.N., J.-T.M. and W.M.-M.; visualization, M.L and W.M.-M.; SEM imaging collection and analysis., J.-T.M.; supervision, W.M.-M.; project administration, W.M.-M.; funding acquisition, W.M.-M. All authors have read and agreed to the published version of the manuscript.

Funding: This research was partially founded by the National Science Foundation REU-Site Award Number: 2150365.

Institutional Review Board Statement: Not applicable.

Informed Consent Statement: Not applicable.

Data Availability Statement: The data are contained within the article.

Acknowledgments: The authors would like to express their sincere appreciation to Preston Larson from the Samuel Roberts Noble Electron Microscopy Laboratory at the University of Oklahoma for help with the Keyence Digital Microscope (VHX-7000 Keyence Ultramicroscope) and with the Thermo-Quattro S-field-emission environmental scanning electron microscope. Many thanks to Sooraj Patel for sharing his deep knowledge of microscopy and for his helpful discussions on the Keyence Digital Microscope. M.L. and W.M.M. gratefully acknowledge the support for this work from the National Science Foundation REU-Site Award Number: 2150365. Many thanks to Zahed Siddique and Shawn Jones for sharing the fume hood (B30 Core-Shared Laboratory) for 3D printing the sample blocks.

Conflicts of Interest: The authors declare no conflicts of interest.

References

1. Cassie, A.B.D.; Baxter, S. Wettability of porous surfaces. *Trans. Faraday Soc.* **1944**, *40*, 546–551. [CrossRef]
2. Wenzel, R.N. Resistance of solid surfaces to wetting by water. *Ind. Eng. Chem.* **1936**, *28*, 988–994. [CrossRef]
3. Xue, C.H.; Jia, S.T.; Zhang, J.; Ma, J.Z. Large-area fabrication of superhydrophobic surfaces for practical applications: An overview. *Sci. Technol. Adv. Mater.* **2010**, *11*, 033002. [CrossRef] [PubMed]
4. Puliyalil, H.; Filipič, G.; Cvelbar, U. Recent advances in the methods for designing superhydrophobic surfaces. *IntechOpen* **2015**, *11*, 311–335.

5. Sung, Y.H.; Kim, Y.D.; Choi, H.J.; Shin, R.; Kang, S.; Lee, H. Fabrication of superhydrophobic surfaces with nano-in-micro structures using UV-nanoimprint lithography and thermal shrinkage films. *Appl. Surf. Sci.* **2015**, *349*, 169–173. [CrossRef]
6. Vandencasteele, N.; Merche, D.; Reniers, F. XPS and contact study of N_2 and O_2 plasma-modified PTFE, PVDF and PVF surfaces. *Surf. Interface Anal.* **2006**, *38*, 526–530. [CrossRef]
7. Kontziampasis, D.; Boulousis, G.; Smyrnakis, A.; Ellinas, K.; Tserepi, A.; Gogolides, E. Biomimetic, antireflective, superhydrophobic and oleophobic PMMA and PMMA-coated glass surfaces fabricated by plasma processing. *Microelectron. Eng.* **2014**, *121*, 33–38. [CrossRef]
8. Barshilia, H.C.; Gupta, N. Superhydrophobic polytetrafluoroethylene surfaces with leaf-like micro-protrusions through Ar+O_2 plasma etching process. *Vacuum* **2014**, *99*, 42–48. [CrossRef]
9. Crick, C.R.; Ismail, S.; Pratten, J.; Parkin, I.P. An investigation into bacterial attachment to an elastomeric superhydrophobic surface prepared via aerosol assisted deposition. *Thin Solid Films* **2011**, *519*, 3722–3727. [CrossRef]
10. Yim, J.H.; Rodriguez-Santiago, V.; Williams, A.A.; Gougousi, T.; Pappas, D.D.; Hirvonen, J.K. Atmospheric pressure plasma enhanced chemical vapor deposition of hydrophobic coatings using fluorine-based liquid precursors. *Surf. Coat. Technol.* **2013**, *234*, 21–32. [CrossRef]
11. Paxson, A.T.; Yagüe, J.L.; Gleason, K.K.; Varanasi, K.K. Stable dropwise condensation for enhancing heat transfer via the initiated chemical vapor deposition (iCVD) of grafted polymer films. *Adv. Mater.* **2014**, *26*, 418–423. [CrossRef]
12. Koo, S.H.; Lee, S.G.; Bong, H.; Kwark, Y.J.; Cho, K.; Lim, H.S.; Cho, J.H. Robust multifunctional superhydrophobic organic–inorganic hybrid macroporous coatings and films. *Polymer* **2014**, *55*, 2661–2666. [CrossRef]
13. Zhu, J.; Zhang, S.; Wang, L.; Jia, D.; Xu, M.; Zhao, Z.; Qiu, J.; Jia, L. Engineering cross-linking by coal-based graphene quantum dots toward tough, flexible, and hydrophobic electrospun carbon nanofiber fabrics. *Carbon* **2018**, *129*, 54–62. [CrossRef]
14. Huang, Y.X.; Wang, Z.; Hou, D.; Lin, S. Coaxially electrospun super-amphiphobic silica-based membrane for anti-surfactantwetting membrane distillation. *J. Membr. Sci.* **2017**, *531*, 122–128. [CrossRef]
15. Rahman, M.A.; Jacobi, A.M. Drainage of frost melt water from vertical brass surfaces with parallel microgrooves. *Int. J. Heat Mass Transf.* **2012**, *55*, 1596–1605. [CrossRef]
16. Kaur, G.; Marmur, A.; Magdassi, S. Fabrication of superhydrophobic 3D objects by Digital Light Processing. *Addit. Manuf.* **2020**, *36*, 101669. [CrossRef]
17. Wang, B.; Chen, J.; Kowall, C.; Li, L. 3D-printed repeating re-entrant topography to achieve on-demand wettability and separation. *ACS Appl. Mater. Interfaces* **2020**, *12*, 35725–35730. [CrossRef] [PubMed]
18. Jafari, R.; Cloutier, C.; Allahdini, A. Momen, Recent progress and challenges with 3D printing of patterned hydrophobic and superhydrophobic surfaces. *Int. J. Adv. Manuf. Technol.* **2019**, *103*, 1225–1238. [CrossRef]
19. He, Z.; Chen, Y.; Yang, J.; Tang, C.; Lv, J.; Liu, Y.; Mei, J.; Lau, W.; Hui, D. Fabrication of polydimethylsiloxane films with special surface wettability by 3D printing. *Compos. Part B Eng.* **2017**, *129*, 58–65. [CrossRef]
20. Credi, C.; Levi, M.; Turri, S.; Simeone, G. Stereolithography of perfluoropolyethers for the microfabrication of robust omniphobic surfaces. *Appl. Surf. Sci.* **2017**, *404*, 268–275. [CrossRef]
21. Tricinci, T.; Terencio, B.; Mazzolai, N.M.; Pugno, F.; Greco, V. Mattoli, 3D Micropatterned Surface Inspired by Salvinia molesta via Direct Laser Lithography. *ACS Appl. Mater. Interfaces* **2015**, *7*, 25560–25567. [CrossRef]
22. Lee, S.-M.; Kwon, T.H. Mass-producible replication of highly hydrophobic surfaces from plant leaves. *Nanotechnology* **2006**, *17*, 3189. [CrossRef]
23. Vandencasteele, N.; Broze, B.; Collette, S.; De Vos, C.; Viville, P.; Lazzaroni, R.; Reniers, F. Evidence of the synergetic role of charged species and atomic oxygen in the molecular etching of PTFE surfaces for hydrophobic surface synthesis. *Langmuir* **2010**, *26*, 16503–16509. [CrossRef]
24. Merchan-Breuer, D.; Murphy, E.; Berka, B.; Echeverria, E.; McIlroy, D.N.; Merchan-Merchan, W. Biodiesel flames as a unique pyrolyzing carbon source for the synthesis of hydrophobic carbon films. *Carbon Lett.* **2021**, *31*, 389–406. [CrossRef]
25. Naha, S.; Sen, S.; Puri, I.K. Flame synthesis of superhydrophobic amorphous carbon surfaces. *Carbon* **2007**, *45*, 1702–1706. [CrossRef]
26. Xiao, L.; Zeng, W.; Liao, G.; Yi, C.; Xu, Z. Thermally and chemically stable candle soot superhydrophobic surface with excellent self-cleaning properties in air and oil. *ACS Appl. Nano Mater.* **2018**, *1*, 1204–1211. [CrossRef]
27. Merchan-Breuer, D.A.; Murphy, E.; Berka, B.; Nova, L.C.M.; Liu, Y.; Merchan-Merchan, W. Synthesis of Carbonaceous Hydrophobic Layers through a Flame Deposition Process. *Appl. Sci.* **2022**, *12*, 2427. [CrossRef]
28. Mansurov, Z.A.; Nazhipkyzy, M. Flame Synthesis of Superhydrophobic Carbon Surfaces. Available online: http://www.kinetics.nsc.ru/kcp/9ISFS/Proceedings/Mansurov.pdf (accessed on 29 January 2022).
29. Yang, L.; Fu, H.; Yang, C.; Tian, W.; Wu, P.; Jiang, W. Carbon soot with arbitrary wettability deposited on solid surface by ethanol flame method. *Colloids Surf. A Physiochem. Eng. Asp.* **2019**, *578*, 123576. [CrossRef]
30. Esmeryan, K.D.; Castano, C.E.; Mohammadi, R.; Lazarov, Y.; Radeva, E.I. Delayed condensation and frost formation on superhydrophobic carbon soot coatings by controlling the presence of hydrophilic active sites. *J. Phys. D Appl. Phys.* **2018**, *51*, 055302. [CrossRef]
31. Elegoo. *Standard Photopolymer Resin*; CANEC2205521501 Datasheet; Elegoo: Shenzhen, China, 2022.
32. Rahman, M.A.; Jacobi, A.M. Experimental study on frosting/ defrosting characteristics of microgrooved metal surfaces. *Int. J. Refigerat.* **2015**, *50*, 44–56. [CrossRef]

33. Zhang, L.; Resasco, D.E. Single-walled carbon nanotubes pillars: A superhydrophobic surface. *Langmuir* **2009**, *25*, 4792–4798. [CrossRef] [PubMed]
34. Liu, H.; Zhang, Z.; Wu, C.; Su, K.; Kan, X. Biomimetic Superhydrophobic Materials through 3D Printing: Progress and Challenges. *Micromachines* **2023**, *14*, 1216. [CrossRef] [PubMed]

Disclaimer/Publisher's Note: The statements, opinions and data contained in all publications are solely those of the individual author(s) and contributor(s) and not of MDPI and/or the editor(s). MDPI and/or the editor(s) disclaim responsibility for any injury to people or property resulting from any ideas, methods, instructions or products referred to in the content.